Unidirectional Hybrid Multilevel Rectifier Family for MV/HV Applications: Analysis and Comparative Evaluation

Jian Liu, *Member, IEEE*, Jayesh Kumar Motwani, *Student Member, IEEE*, Di Zhang, *Senior Member, IEEE*, Dong Dong, *Senior Member, IEEE*

***Abstract*- Medium voltage (MV) and high voltage (HV) rectifiers demonstrate lower cost and volume as well as reversal power protection compared to the bidirectional counterparts in the unidirectional AC/DC applications, such as HVDC transmission, MVDC shipboard system, subsea oil and gas production power systems, etc. Traditional modular multilevel converter (MMC) is good candidate, but suffers from large number of submodules (SMs) and capacitor size. Recently, the hybrid multilevel rectifiers (HMRs) consisting of the HV diode and MMC structure have evolved and gained significant interests. The HV diode could replace the SMs in MMC, implying improved power density and efficiency. In this paper, three typical HMR topologies are selected, and each of them uses a different configuration and offers unique advantages. Therefore, this paper presents the operation principles and comparative performance evaluation of these HMRs based on key metrics such as device number, capacitor energy storage requirement, and semiconductor losses. In this way, the favorable working conditions of these HMRs could be identified, and the most suitable applications for each configuration could be suggested. The presented analysis can provide a point of reference and a useful framework for the future developments of HMRs.**

***Index Terms*- Unidirectional rectifier, hybrid modular multilevel rectifier (HMMR), flying-capacitor HMMR, asymmetrical alternate arm rectifier, operation principle, performance comparison.**

I. Introduction

The use of unidirectional high-voltage (HV) and medium-voltage (MV) rectifiers is preferred in applications where power only flows from the AC to the DC side. These applications include the point-to-point HVDC transmission for renewable energy [1, 2] and the active front-end (AFE) converters in variable speed drive systems [3, 4]. In addition, some non-conventional applications such as subsea oil and gas production power systems [5] as well MVDC shipboard [6] require rectifier topologies with higher power density and efficiency. Bidirectional converters are more complex and expensive than unidirectional ones in these non-regenerative systems. Furthermore, unidirectional rectifiers are more favorable for protecting the primary power source against power flow reversals.

The simplest and most well-known solution for the unidirectional medium-voltage rectifier is the passive diode rectifier (DR) and the multi-pulse rectifier based on phase-shifting transformer arrangements [7]. This method features a simple structure, lower cost, and smaller volume, which makes it promising for offshore wind power transmission [8]. However, the use of passive devices in DR also presents some challenges. First, the low-frequency transformers (LFT) used on the grid side are quite bulky. Second, harmonic compensation equipment is necessary to meet the total harmonic distortion (THD) requirement. Third, the DR is unable to operate in weak grids and cannot ride through the low voltage on the AC side.

Multilevel converters have become a competitive alternative to passive diode rectifiers due to their ability to decrease harmonics and provide fully controlled active and reactive power. Some typical multilevel converters include the neutral point clamped (NPC) converter, the flying capacitor converter (FCC), and the cascade H-bridge (CHB) converter. In the case of unidirectional power flow, the rectifier version of the five-level active neutral point clamped (ANPC) converter using SiC MOSFET and Si diode was proposed in [12-14]. However, to increase the voltage rating, more voltage levels are needed, which can make busbar design difficult due to the larger parasitic inductance of the commutation loop. The CHB could avoid this issue by using series connected submodules (SMs), whereas the back-end high frequency isolated DC/DC converters are required to interface MVDC with series output or LVDC with parallel output [15-17]. This kind of structure is usually referred to as solid-state transformer (SST). SST can provide higher power density and efficiency over traditional line-frequency transformer (LFT) based rectifier. Therefore, SST is very promising for isolated rectifier applications. Similarly, the modular multilevel converter (MMC) has same benefit of CHB, but can be used in transformerless applications [18], [19]. Although the MMC offers good scalability and natural redundancy, it requires a large number of low-voltage devices and SM capacitors with a large volume [20].

Various hybrid multilevel converters (HMCs) have been proposed by combining the HV switch and chain-link (CL) structure in MMC, to achieve a trade-off between traditional multilevel converters and MMC [21-25]. The typical topologies include the alternate arm converter (AAC) [23],

This work was supported by the National Science Foundation under Grant 2022397. (Corresponding author: Dong Dong.)

Jian Liu is with Delta Electronics Inc., Durham, NC 27709 USA, (email: jian.h.liu@deltaww.com).

Jayesh Kumar Motwani and Dong Dong are with the Center for Power Electronics Systems, Virginia Polytechnic Institute and State University, Blacksburg, VA 24060 USA, (e-mail: jayeshkmotwani@vt.edu; dongd@vt.edu).

Di Zhang is with the Naval Postgraduate School, Monterey, CA 93943-5155 USA (e-mail: zhangdi@ieee.org).

and three-level hybrid modular multilevel converter (HMMC) [24]. They can address one or more issues of traditional MMC.

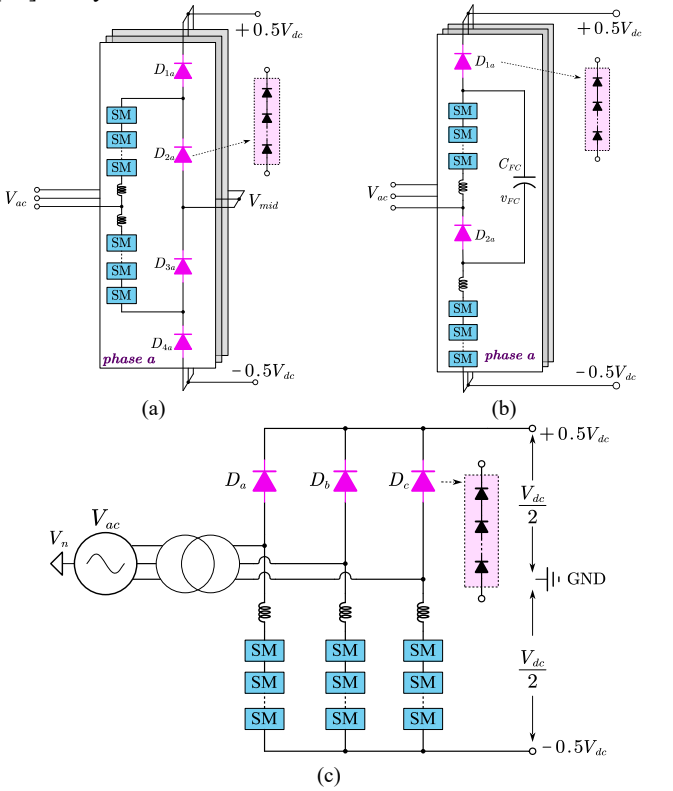

Fig. 1 Three typical HMR topologies, (a) HMMR, (b) FC-HMMR, (c) AAAR.

However, these converters are bidirectional using the active HV switch, which still has the concern of voltage sharing based on low voltage device. To further reduce the cost and construction difficulty of the HV switch, the hybrid multilevel rectifiers (HMRs) are proposed by replacing the active HV switch with the HV diode. Because diode does not need the gate driver unit and the simple passive snubber based voltage balancing is sufficient. The most representative topologies include the hybrid modular multilevel rectifier (HMMR) [26-28], the flying-capacitor HMMR (FC-HMMR) [29], and the asymmetrical alternate arm rectifier (AAAR) [30] as shown in Fig. 1. The combination of HV diode and CL structure gets rid of the harmonic and voltage upregulation concerns of traditional DR, while reducing the SM requirement of pure MMC. However, diode does not have the current interruption capability, which means non-unity power factor (PF) operation is different from HMCs, which may bring more penalty and limit the suitable applications.

Up to now, there is a significant gap in the available literature about the comparative evaluation of these HMRs to identify the suitable applications. Therefore, this paper aims to fill this gap by providing such a comparison, and the main contributions of this paper are summarized as below.

- Introduce three MV and HV unidirectional HMRs. Both the unity and non-unity power factor (PF) operation principles are explained.
- The control scheme and CL energy balancing strategy of three topologies are illustrated.
- A detailed analysis of the performance of three HMRs is provided to identify their advantages and limitations. This will help people to choose the most appropriate topology for their specific application.
- The simulation and experimental results are provided to validate the effectiveness of these topologies.

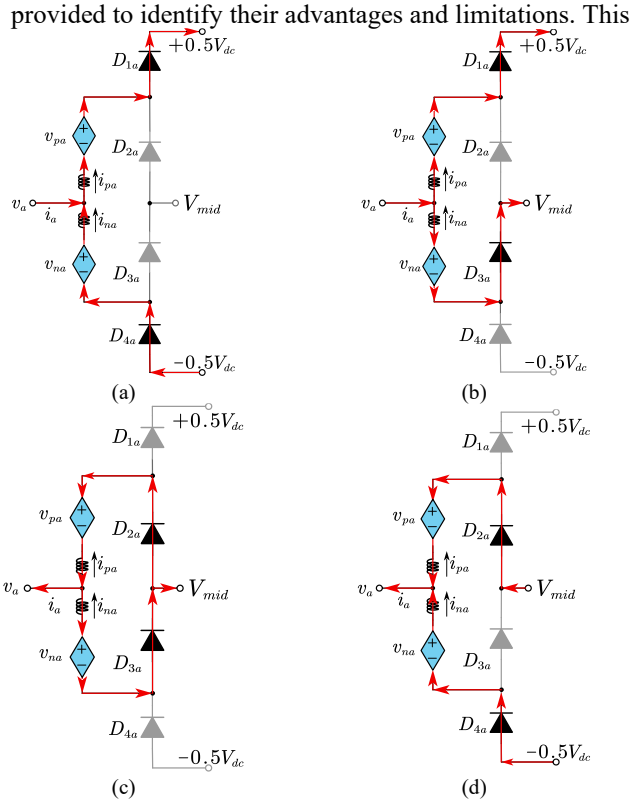

Fig. 2 Four working states of single phase HMMR, (a) *PN* state, (b) *PZ* state, (c) *ZZ* state, (d) *ZN* state.

The paper is structured as follows. Section II gives an overview of three unidirectional HMRs, along with their corresponding operation principles. In Section III, a performance comparison between the traditional MMC and three other considered topologies at different PFs is conducted. Based on the analysis, the benefits and limitations of each HMR are highlighted, which will help to identify their suitable applications. Section IV presents the simulation and experimental results of a scale-down prototype, which is used to validate HMMR and FC-HMMR. Finally, the concluding remarks based on the findings of our study are given in Section V.

II. Operation Principles and Control Method

This chapter introduces and discusses the basic working principle of three HMRs. Firstly, the AC side voltages and currents are defined as follows,

$$v_a = V_{ac}\sin(\omega t),\ i_a = I_{ac}\sin(\omega t + \varphi) \tag{1}$$

where V_{ac} and I_{ac} represent the amplitude of AC voltage and current, respectively. The angular frequency is denoted by ω, whereas the phase angle difference between current and voltage is given by φ, which determines the PF value. The modulation index M is defined as $2V_{ac}/V_{dc}$.

A. Operation of HMMR

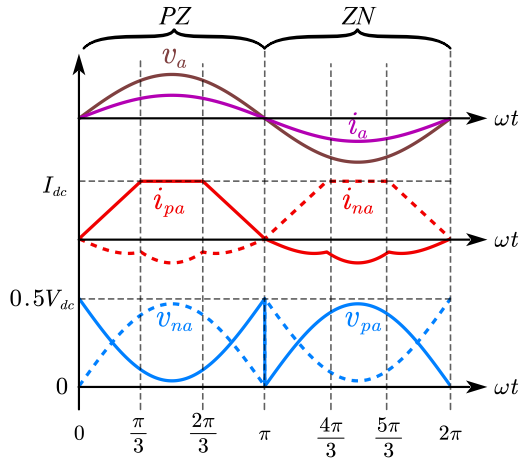

Fig. 3 Single-phase CL current and voltage waveforms of HMMR at unity PF.

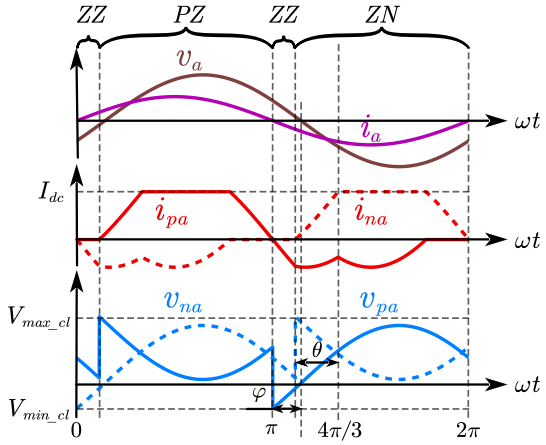

Fig. 4 Single-phase CL current and voltage waveforms of HMMR at non-unity PF.

The topology of the three-phase HMMR is given in Fig. 1(a). Four series-connected HV diodes are connected between the DC terminals, and two CLs are connected between the AC side and the HV diodes, respectively. Three phase midpoints are connected as the voltage potential V_{mid}. It should be noted that each CL contains N_{h} half-bridge (HB) SMs and N_{f} full-bridge (FB) SMs. Besides, each SM has a floating capacitor C_{sm} at voltage V_{sm}. The total voltages across the upper and lower CLs are denoted by v_{pa} and v_{na}, respectively, while the upper and lower arm currents are denoted as i_{pa} and i_{na}, respectively.

Considering the symmetrical structure of HMMR, phase *a* is taken as an example to illustrate the operation. Fig. 2 demonstrates the four working states (*PN*, *PZ*, *ZZ*, and *ZN*) of a single-phase HMMR, which are determined by the current polarity of i_{pa} and i_{na}. Then the corresponding upper and lower CL voltages can be calculated based on the connection structure.

$$\begin{aligned}
&v_{pa}=0.5V_{dc}-v_a,\ v_{na}=0.5V_{dc}+v_a && (i_{pa}>0,i_{na}>0,PN)\\
&v_{pa}=0.5V_{dc}-v_a,\ v_{na}=v_a-V_{mid} && (i_{pa}>0,i_{na}<0,PZ)\\
&v_{pa}=V_{mid}-v_a,\ v_{na}=v_a-V_{mid} && (i_{pa}<0,i_{na}<0,ZZ)\\
&v_{pa}=V_{mid}-v_a,\ v_{na}=0.5V_{dc}+v_a && (i_{pa}<0,i_{na}>0,ZN)
\end{aligned} \tag{2}$$

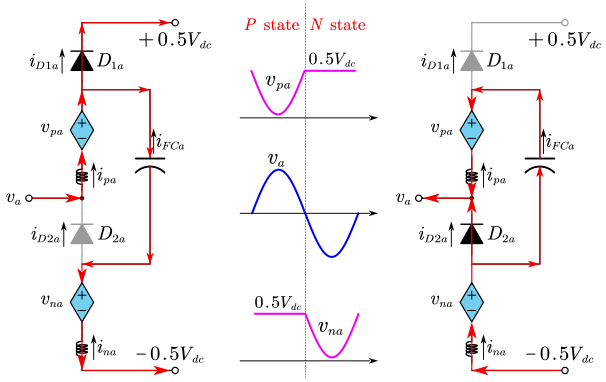

Fig. 5 Two working states of single-phase FC-HMMR.

The trapezoidal arm current allocation in Fig. 3 is designed to enable natural switching between *PZ* and *ZN* states, which helps to achieve minimum CL voltage stress and 50% SM reduction compared to traditional MMC. To ensure the arm current polarity for the corresponding states, a modulation index limitation is calculated at the unity PF, as shown in (3). This indicates that the HMMR is feasible for the most common boost rectifier operation.

$$M=\frac{2V_{ac}}{V_{dc}}<\frac{2}{\sqrt{3}}\approx 1.15 \tag{3}$$

As for the non-unity PF, the *PN* or *ZZ* states could be used during the non-overlap period to reduce the extra SM number. The detailed current allocation has been introduced in a previous study [26], so it will not be discussed here. An example with the transition of *ZZ* states is presented in Fig. 4. Then, the corresponding CL voltage stress should be calculated as follows:

$$\begin{aligned}
&V_{max_cl}=0.5V_{dc}+V_{ac}\sin(\gamma),\\
&\theta=\operatorname{asin}\left(\frac{I_{dc}}{I_{ac}}\right),\ \gamma=\theta+\varphi-\frac{\pi}{3}\\
&V_{min_cl}=-V_{ac}\sin\varphi
\end{aligned} \tag{4}$$

B. Operation of FC-HMMR

Fig. 1(b) shows the topology of FC-HMMR, which utilizes two CLs, two HV diodes, and one HV flying capacitor per phase. The currents flowing through them are defined as i_{pa}, i_{na}, i_{D1a}, i_{D2a}, i_{FCa}, respectively. The rated flying capacitor voltage V_{FCa} is set as $0.5V_{\text{dc}}$. According to the conduction of two diodes, there are two working states of FC-HMMR as shown in Fig. 5. The corresponding CL voltages and currents can be calculated using (5) and (6).

$$\begin{aligned}
&v_{pa}=0.5V_{dc}-v_a,\ v_{na}=V_{dc}-v_{FCa} && (i_{d1a}>0,i_{d2a}=0,P)\\
&v_{pa}=v_{FCa},\ v_{na}=0.5V_{dc}+v_a && (i_{d1a}=0,i_{d2a}>0,N)
\end{aligned} \tag{5}$$

$$\begin{aligned}
&i_{pa}=i_a,\ i_{na}=i_{FCa}=i_{D1a}-i_a && (P\text{ state})\\
&i_{pa}=-i_{FCa}=i_{D2a}+i_a,\ i_{na}=-i_a && (N\text{ state})
\end{aligned} \tag{6}$$

It is important to note that two diodes cannot be turned on simultaneously to prevent voltage fluctuations in the flying capacitor. Moreover, if the switching point between the P and N states coincides with the zero-crossing point of the AC voltage, the maximum voltage across the CL is effectively reduced to only $0.5V_{\mathrm{dc}}$.

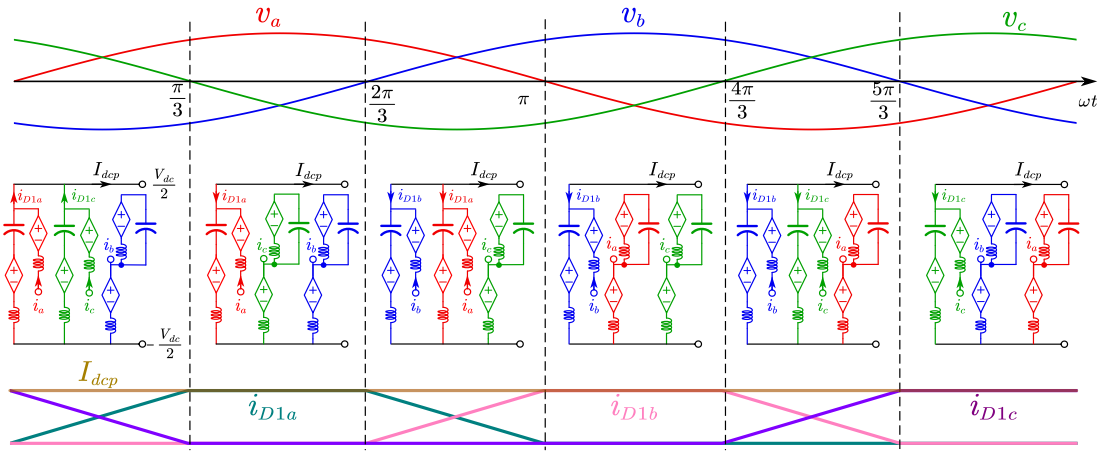

Fig. 6 Three-phase configuration of FC-HMMR at unity PF.

By applying these two states to three phases, we can obtain a three-phase configuration with six segments in a single line cycle, as illustrated in Fig. 7. It can be observed that the positive DC bus current is equal to the D_1 current of one phase or two parallel phases in each segment, as shown in (7).

$$I_{dcp}=\begin{cases} i_{D1a}+i_{D1c},\ \omega t\in[0,\pi/3) \\ i_{D1a},\ \omega t\in[\pi/3,2\pi/3) \\ i_{D1a}+i_{D1b},\ \omega t\in[2\pi/3,\pi) \\ i_{D1b},\ \omega t\in[\pi,4\pi/3) \\ i_{D1b}+i_{D1c},\ \omega t\in[4\pi/3,5\pi/3) \\ i_{D1c},\ \omega t\in[5\pi/3,2\pi) \end{cases} \tag{7}$$

To maintain a constant total positive DC bus current with minimal ripple, a trapezoidal current allocation could be used here to design the current distribution among three phases, as shown in the bottom of Fig. 6. For example, i_{D1a} could be expressed in (8).

$$i_{D1a}=\begin{cases} I_{DC}\cdot 3\omega t/\pi,\ \omega t\in[0,\pi/3) \\ I_{DC},\ \omega t\in[\pi/3,2\pi/3) \\ I_{DC}\cdot 3(\pi-\omega t)/\pi,\ \omega t\in[2\pi/3,\pi) \\ 0,\ \omega t\in[\pi,2\pi) \end{cases} \tag{8}$$

Based on the power transfer, the amplitude of the DC side current can be easily derived using (9). It is noteworthy that the shape of i_{D1a}, i_{D1b}, and i_{D1c} remains trapezoidal even as the modulation index and PF vary, except for the variable amplitude I_{dc}.

$$I_{dc}=\frac{MI_{ac}\cos\varphi}{4} \tag{9}$$

As a result, when the modulation index and PF changes, FC-HMMR could always maintain the P (or N) and when AC voltage is positive (or negative). Compared to HMMR, which is affected by non-unity PF, the CL voltage stress of FC-HMMR does not change when PF varies. Additionally, there is no modulation index limitation for FC-HMMR, making it a feasible option for a buck rectifier with the FB SM. In this case, the voltage stress can be expressed in (10). Combining the current relationship given in (6), the corresponding CL and FC currents can be plotted as shown in Fig. 7.

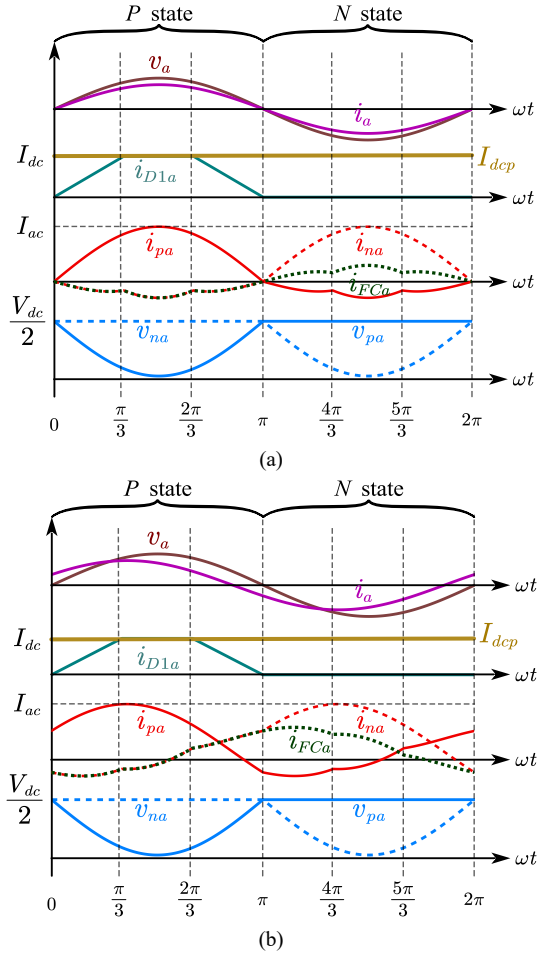

Fig. 7 Current pattern of CLs and flying capacitor at (a) unity PF and (b) PF = 0.8.

$$V_{max\_cl}=0.5V_{dc},\ V_{min\_cl}=0.5V_{dc}-V_{ac} \tag{10}$$

D. Operation of AAAR

In Fig. 1(c), AAAR is derived with three HV diodes replacing three upper CLs in the traditional MMC. This asymmetrical design can reduce the total number of SMs. The diode conducts when the respective instantaneous phase voltage is highest among the three phases. Therefore, there are

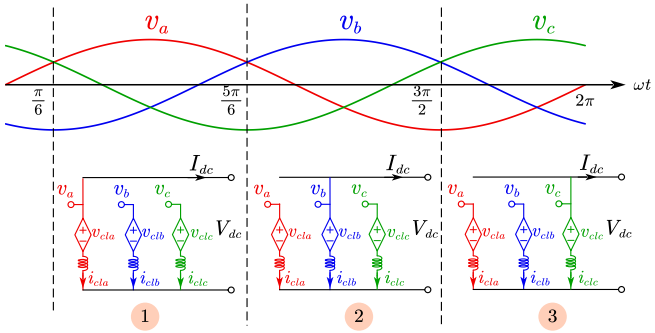

Fig. 8 Three working states of AAAR in one line cycle.

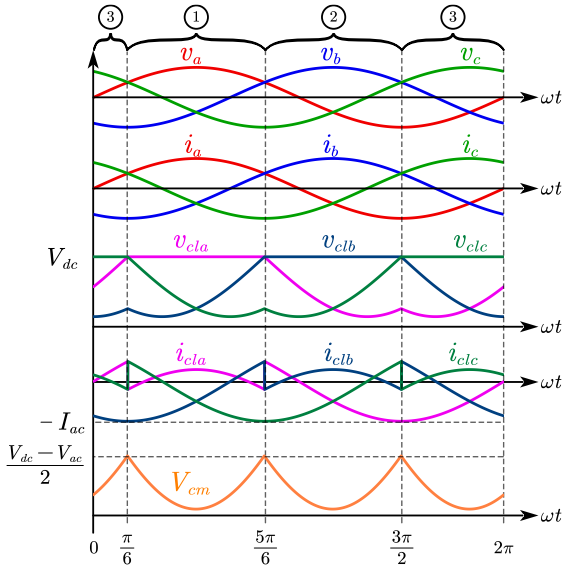

Fig. 9 Three-phase CL voltages and currents waveforms of AAAR.

three different working states for AAAR in one line cycle, as shown in Fig. 8. The three-phase CL voltages and currents in state 1 could be expressed in (11) and (12), respectively.

$$\begin{cases} v_{cla} = V_{dc} \\ v_{clb} = V_{dc} - v_a + v_b \\ v_{clc} = V_{dc} - v_a + v_c \end{cases}, \omega t \in \left[\frac{\pi}{6}, \frac{5\pi}{6}\right) \tag{11}$$

$$\begin{cases} i_{cla} = i_a - I_{DC} \\ i_{clb} = i_b \\ i_{clb} = i_c \end{cases}, \omega t \in \left[\frac{\pi}{6}, \frac{5\pi}{6}\right) \tag{12}$$

Unlike HHMR and FC-HMMR, the common-mode voltage V_{cm} between the DC side midpoint and the three-phase neutral point of AAAR is non-zero. For instance, in state 1, it can be calculated using (12).

$$V_{cm} = 0.5V_{dc} - v_a,\ \omega t \in [\pi/6, 5\pi/6) \tag{13}$$

The expressions for the other two states can be derived similarly, which can plot the three-phase CL voltages and currents in Fig. 9. It can be observed that the maximum voltage stress remains the same as the traditional MMC at V_{dc}. However, there is a large third-order harmonic in the common mode voltage. This means that AAAR cannot operate in single-phase mode, and a three-phase transformer with the

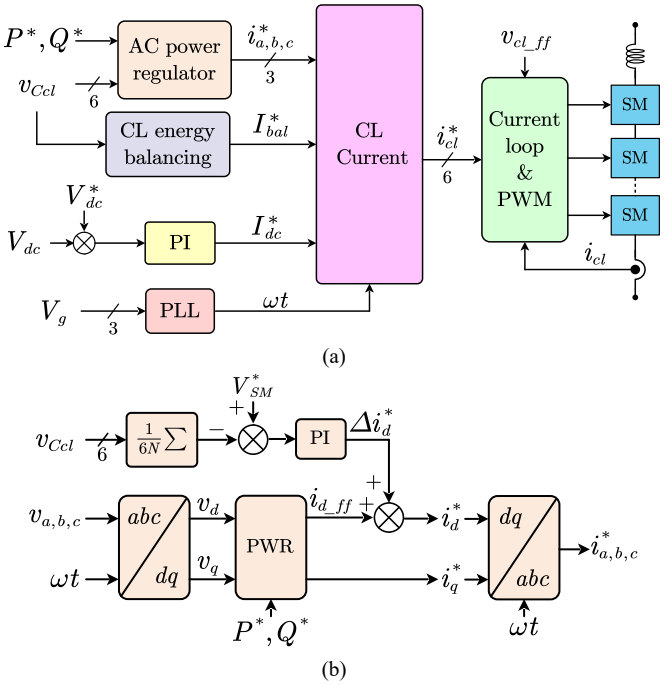

Fig. 10 (a) Basic control schemes of HMRs, (b) AC side power control block and sum energy balancing.

neutral point insulation reinforcement, as shown in Fig. 1(c), is necessary to block such common mode voltage.

D. Control Schemes of Three HMRs

Despite the different configurations and operation principles of the three HMRs, their basic control schemes remain the same. The only difference between them is the method used to balance the CL energy.

As illustrated in Fig. 10, the control scheme comprises the AC side control, the DC side control, and the CL energy balancing, which generate different components of the CL current reference. For instance, the AC side control, as shown in Fig. 10(b), computes the AC input current reference based on the active and reactive power demand. The active current should be adjusted to regulate the total energy stored in HMR as well. On the other hand, the DC side control generates the DC output current reference.

The CL energy balancing for HMMR is achieved by injecting circulating current, whereas for FC-HMMR and AAAR, the DC current amplitude for each phase can be independently regulated for balancing purposes.

After synthesizing the CL current reference based on the operation principle in each state, the current loop regulator is responsible for tracking the reference using repetitive control. The resulting output, combined with the feedforward CL

voltage calculation, generates the CL reference output voltage, denoted as v_{cl}^*. The low-level control, on the other hand, is responsible for multilevel modulation and balancing of individual capacitor voltages.

With the increasing number of SMs, traditional centralized control limit the modularity and expandability due to the heavy computational burden [31]. Therefore, the distributed control has been discussed a lot in MMC family [32-34],

TABLE I
Specifications of MV AFE

Description	Symbol	Value
Input three-phase Line-voltage (RMS)	$V_{LL\ rms}$ (kV)	13.8
Input frequency	f_{in} (Hz)	60
Output DC bus voltage	V_{DC} (kV)	24
Rated power	S (MVA)	5
PF	PF	0 to 1
SM capacitor voltage	V_{SM} (kV)	1.1
SM capacitor ripple	ε	10%

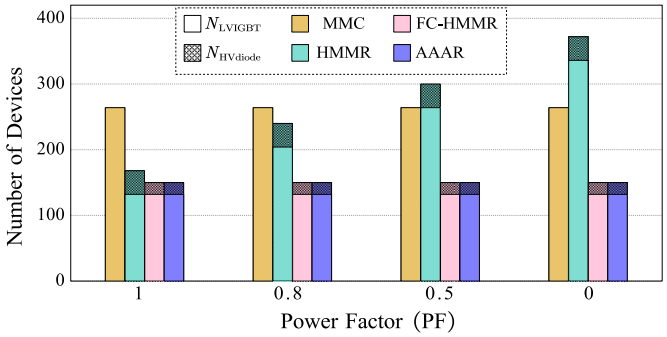

Fig. 11 Number of devices for four topologies at four different PFs.

which can be easily transferred to HMRs as well. More detailed aspects such as control task allocation, clock synchronization as well as the communication fault tolerant operation still deserves more future investigation.

III. Performance Comparison of Four Topologies

To identify the strengths and weaknesses of each topology, it is essential to design the converters under different operating conditions. This approach ensures a fair comparison between the different topologies. Table I gives the design parameters for the medium voltage rectifier.

A. CL voltage and Device Number

The arm voltage stress is directly proportional to the device number. In this study, the Infineon IGBT module FF300R17KE4 [35] is utilized as the SM power device, which has a maximum collector-emitter voltage of 1.7 kV and can sustain a continuous DC collector current of up to 300A. As for the HV diode stack, the 6.5 kV diode module from IXYS (W0790LG650) [36] is selected here to reduce the total device number.

The number of SMs in each arm is selected so that the DC link capacitor voltage V_{SM} does not exceed 1.1 kV, and the HB SM number N_{HB} and FB SM number N_{FB} could be calculated as below.

$$N_{FB} = \frac{|V_{min\_cl}|}{V_{SM}}, N_{HB} = \frac{V_{max\_cl}}{V_{SM}} - N_{FB} \tag{14}$$

As for the diode requirement, it is related to the total blocking voltage V_{br} at off state. Supposing a blocking utilization factor of 70%, the diode number could be expressed in (14).

$$N_{diode\_HMMR} = \frac{V_{br\_HMMR}}{V_{rv} * 70\%} \tag{15}$$

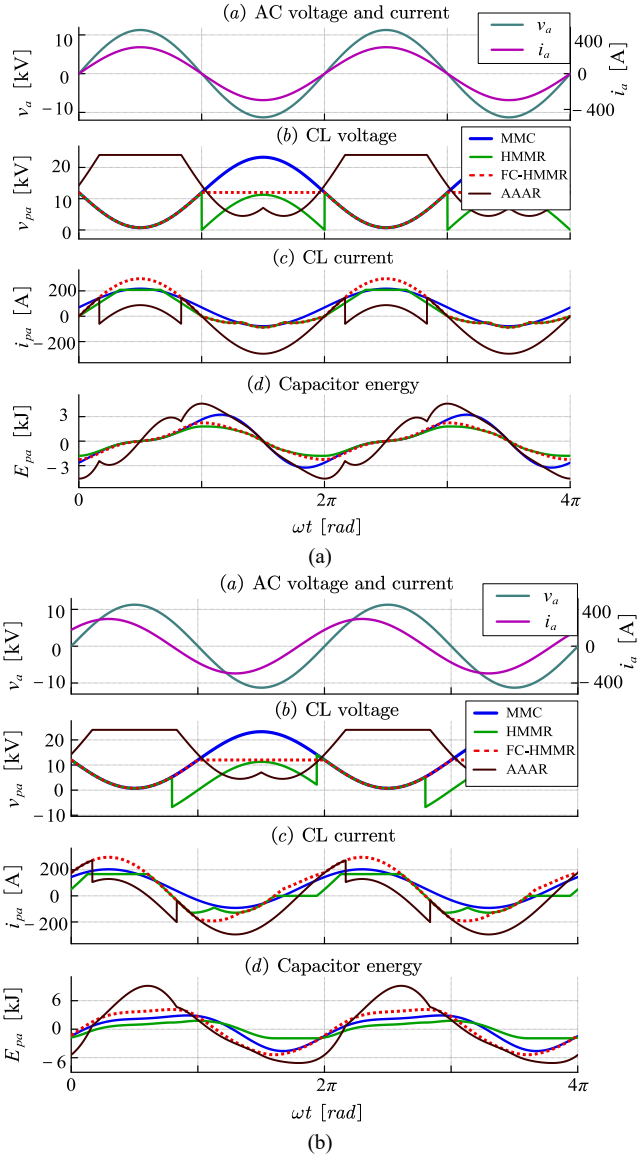

Fig. 12 Ideal waveforms of four topologies at (a) PF = 1 and (b) PF = 0.8.

Therefore, the device number at different PFs is given in Fig. 11. It can be observed that both FC-HMMR and AAAR have lower device number compared to MMC at any PF. Whereas HMMR has a smaller number of devices at only the high PF range. This is because HMMR must use the ZZ state during the overlap period. The lower PF means longer duration of ZZ state, which means lower V_{min_cl} and more FB SMs.

B. Capacitor Energy Storage

In MMC, capacitors are critical components that directly impact power density and cost. The energy storage per unit apparent power E_{unit}, is determined by the energy deviation per CL ΔE, and the capacitor voltage ripple coefficient ε. For example, the E_{unit} for 6 CLs in MMC, HMMR, and FC-HMMR could be expressed as,

$$E_{unit(\text{MMC, HMMR})} = 6N\frac{C_{SM}{V_{SM}}^2}{2S} = \frac{3\Delta E}{2\varepsilon S} \tag{16}$$

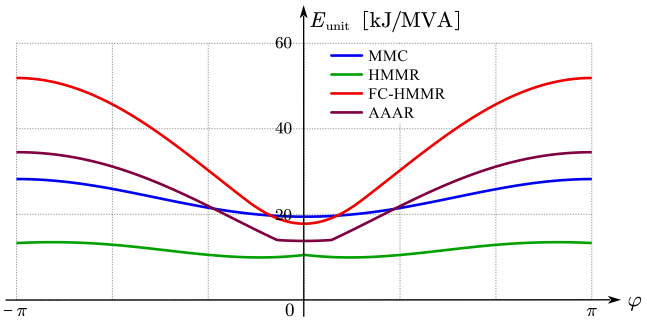

Fig. 13 Relationship between the required capacitor energy storage and phase angle of topologies with ε of 10%.

FC-HMMR needs the extra flying capacitor, which has the same energy deviation as each CL. Then the total capacitor energy storage for FC-HMMR should be calculated as,

$$E_{unit(\text{FC-HMMR})} = 9N\frac{C_{SM}{V_{SM}}^2}{2S} = \frac{9\Delta E}{4\varepsilon S} \tag{17}$$

Since AAAR has only 3 CLs, the energy storage should be calculated by half.

$$E_{unit(\text{AAAR})} = 3N\frac{C_{SM}{V_{SM}}^2}{2S} = \frac{3\Delta E}{4\varepsilon S} \tag{18}$$

Considering the complicated analytic expression of different converters, the numerical method is utilized here. The instantaneous CL energy fluctuation could be calculated by the integral of CL output power.

$$E_{CL} = \int (v_{pa} i_{pa})\, dt \tag{19}$$

The waveforms of CL voltages and currents as well as the corresponding calculated energy from (19) could be plotted in Fig. 12. It can be seen that at the unity PF, HMMR has the lowest capacitor energy ripple, which means the required capacitor energy storage is lowest. Using this method, the phase angle changes from –π to π, and the variation of E_{unit} could be obtained and presented in Fig. 13. The same capacitor voltage ripple coefficient ε is assumed for all topologies of 10%. In terms of capacitor size, HMMR has the best performance among the four topologies at any PF. While AAAR and FC-HMMR are superior to MMC only at the high PF range.

C. Semiconductor Losses

The semiconductor losses consist of conduction losses P_{con} and switching losses P_{sw}. The former is caused by the forward voltage drop of IGBTs and diode stacks, which could be calculated in (20). For simplification, the on-state voltage drop of the IGBT and its antiparallel diode of each IGBT module are assumed to be the same.

$$P_{con} = \frac{N_{CL}}{2\pi}\int_0^{2\pi} (N_{sm} \cdot v_{f\_IGBT} \cdot |i_{IGBT}|)\, d(\omega t) + \frac{N_{CL}}{2\pi}\int_0^{2\pi} (N_{diode} \cdot v_{f\_diode} \cdot i_{diode})\, d(\omega t) \tag{20}$$

where N_{sm} is the number of devices in the conduction path of each CL, and $v_{\text{f\_IGBT}}$ refers to the on-state voltage drop of IGBT at the current i_{IGBT}. N_{diode} is the number of devices in the conduction path of each stack, and $v_{\text{f\_diode}}$ refers to the on-state voltage drop of the diode at the current i_{diode}. N_{cl} denotes the total number of CL, which equals 6 for MMC, HMMR, and FC-HMMR. As for AAAR, N_{cl} equals 3.

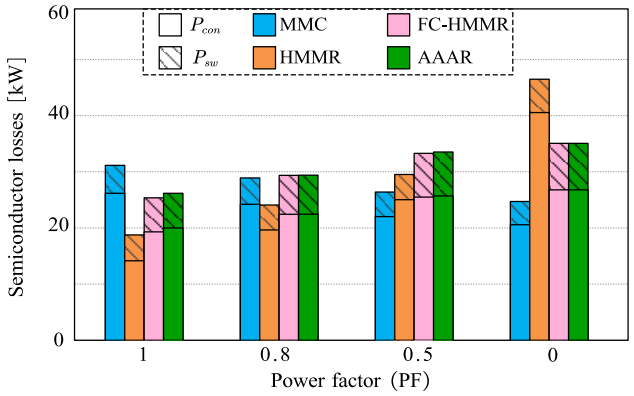

Fig. 14 Power losses of four topologies at four PFs.

Each state change of a SM results in a one-time turn-on loss (e_{on}), turn-off loss (e_{off}) of the IGBT, and reverse recovery loss (e_{rec}) of the antiparallel diode. To calculate the equivalent value normalized to the reference voltage $v_{\text{CE,ref}}$ in datasheet, the SM capacitor ripple is disregarded. The CL switching losses P_{sw} are then summed up within one line cycle.

$$P_{sw\_cl} = \frac{\omega}{2\pi}\sum_{\gamma=1}^{N_{sw}}\left\{\frac{V_{SM}}{v_{CE,ref}} \cdot e_{on(off)}(i_{IGBT}) + \frac{V_{SM}}{v_{F,ref}} \cdot e_{rec}(i_{IGBT})\right\} \tag{21}$$

The reverse recovery losses of the HV diodes are neglected here due to the low frequency and zero current commutation in HMMR and FC-HMMR.

In order to perform a fair comparison, the same switching frequency and device junction temperature is set to be same for all topologies. Then the total power losses of four topologies are presented in Fig. 14. In order to make a fair comparison, the It can be observed that HMMR has the lowest power losses in the high PF range, while MMC has lower losses in the low PF range. FC-HMMR and AAAR have higher conduction losses as PF reduces due to the increased rms value of CL currents.

D. AC Low Voltage Ride Through and DC Fault Ride Through

The AC low voltage ride-through capability is a critical requirement for converters that interface with the MV/HV grid in the event of an AC side fault. Common AC side faults include symmetrical three-phase low-voltage events and asymmetrical single-phase low-voltage events.

In the event of a symmetrical AC fault, all four topologies could handle this fault by reducing the active power accordingly. Furthermore, there will be no current ripple on the DC side due to the absence of negative sequence components. However, the non-reactive power injection is limited for HMMR due to more required devices.

Similar to the traditional HB-MMC, HMMR, FC-HMMR, and AAAR with only HB SMs lack the dc-fault blocking capability. In the event of a fault, the fault current will increase rapidly through the antiparallel diode of each HB SM. Thus, the arm inductor must be designed to limit the current rise rate. In order to protect the system, one way is using the DC circuit breaker or the embedded DC breaker structure [37], [38]. Another way is using the bipolar SM, like the FB circuit, to block the AC side voltage. In the event of a fault, all devices in each FB SM should be turned off. Consequently, the DC-link capacitors of the FB SMs in each arm will appear as serially connected voltage sources, with a polarity opposite to the direction of the fault current flowing from the AC side.

TABLE II
Performance Summary of Four Topologies.

Terms		MMC	HMMR	FC-HMMR	AAAR
PF (1)	Device Number	1 p.u.CL	0.5 p.u. CL + 0.14 p.u. diode	0.5 p.u. CL + 0.07 p.u. diode	0.5 p.u. CL + 0.07 p.u. diode
	Cap energy	1 p.u.	0.54 p.u.	0.92 p.u.	0.71 p.u.
	Power losses	1 p.u.	0.6 p.u.	0.81 p.u.	0.84 p.u.
PF (0.5)	Device Number	1 p.u.CL	1 p.u. CL + 0.14 p.u. diode	0.5 p.u. CL + 0.07 p.u. diode	0.5 p.u. CL + 0.07 p.u. diode
	Cap energy	1 p.u.	0.5 p.u.	1.77 p.u.	1.2 p.u.
	Power losses	1 p.u.	1.12 p.u.	1.26 p.u.	1.27 p.u.
PF range		Any PF	High PF	Any PF	Any PF
Transformer necessity		No	No	No	Yes
Symmetrical AC fault ride-through		Yes	Yes	Yes	Yes
Asymmetrical AC fault ride-through		Yes	Yes	Yes	No
DC fault blocking		Yes with FB			
Recommended applications		Low PF (STATCOM)	High PF (AFE, HVDC)	Wide PF (FCS, datacenters)	Wide PF (OWFs)

For HMMR and FC-HMMR, the required FB SMs per CL should be

$$N_{\text{FB\_DC\_fault(HMMR, FC-HMMR)}} = \frac{\sqrt{3}V_{ac}}{2V_{SM}} \tag{22}$$

While for AAAR, only single CL is connected to withstand the AC voltage, which indicates the FB SM number in (23).

$$N_{\text{FB\_DC\_fault(AAAR)}} = \frac{\sqrt{3}V_{ac}}{V_{SM}} \tag{23}$$

Therefore, HMMR already with FB SMs can help reduce the extra number of SMs required for DC fault protection.

E. Performance Summary

According to the previous comparison, the device number, capacitor energy storage as well as power losses of four topologies can be summarized in Table II. It is apparent that in the high PF range, the HMMR demonstrates highest power density and efficiency due to smaller capacitor size and lower power losses. Therefore, it more preferred in the applications such as AFE in variable speed drive systems or point-to-point HVDC transmission. It can be also used as the MVDC rectifier for the marine electrical distribution system, where no regeneration is possible [39].

When low PF operation is necessary to support the grid, the significantly increased number of devices makes the HMMR an unfavorable solution. Conversely, FC-HMMR and AAAR do not require additional devices and thus provide a better option. While the capacitor energy ripple in these topologies may be higher than that of the MMC, the total apparent power could be reduced accordingly to ensure that the capacitor voltage ripple remains within the permissible limit. Moreover, considering the insulation of flying capacitor and the unnecessity of transformer, the FC-HMMR is more desired for MV applications such as front-end converter for electrical vehicle fast charging station (FCS) and datacenters [28], [40], [41]. Whereas AAAR is suitable for HV case like offshore wind farms (OWFs), where the HV transformer has been employed for each farm [39].

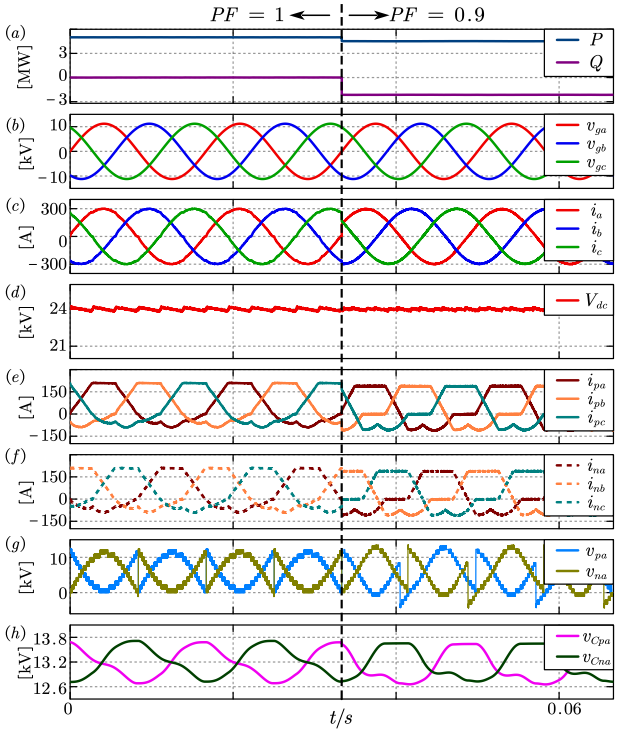

Fig. 15 Steady-state simulation waveforms of HMMR when PF = 1 and 0.9, (a) delivered active and reactive power, (b) AC grid side voltages, (c) AC side currents, (d) DC voltage, (e) three-phase upper CL currents, (f) three-phase lower CL currents, (g) phase *a* upper and lower CL output voltages, (h) phase *a* upper and lower CL capacitor voltages.

However, in some applications of pure reactive power generation, such as the Static Synchronous Compensator (STATCOM), the traditional MMC remains the best candidate due to the large number of devices required for HMMR and the issue of large capacitors faced by FC-HMMR.

IV. Simulation And Experimental Results

A. Simulation Results of Steady State

In Fig. 15, steady-state operation results of HMMR are shown at a constant apparent power of 5 MVA and PF of 1 and 0.9. The low harmonics in the input AC current are due to the multilevel output of CL, as shown in Fig. 15(g). With the help of repetitive control of the current loop [25], the CL currents in Fig. 15(e) and (f) match the designed pattern given in Fig. 4 and Fig. 5. Additionally, due to the balancing control, the CL capacitor voltage is well-balanced and the ripple amplitude changes slightly at different PF, as depicted in Fig. 15(h). To mitigate voltage ripple, the SM capacitance CSM was chosen as 4.5 mF for HMMR.

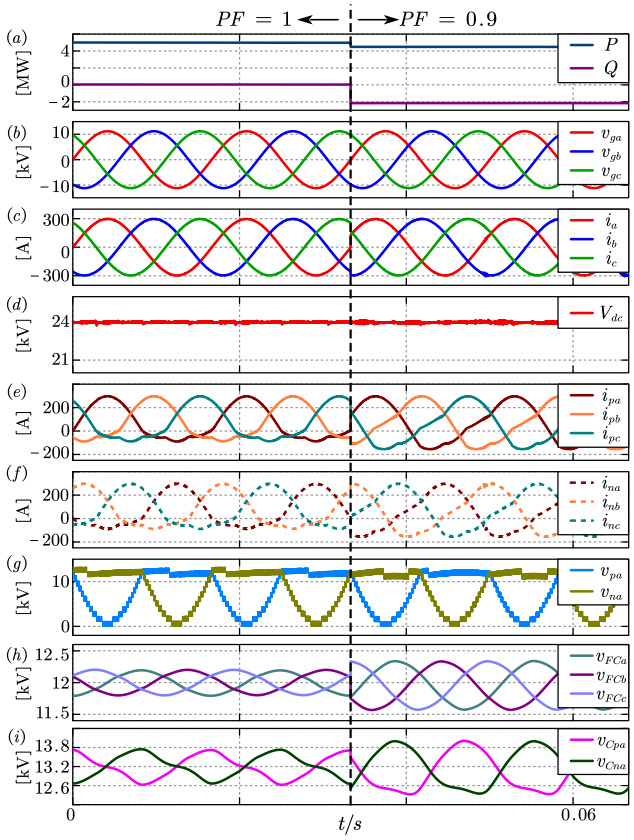

Fig. 16 Steady-state simulation waveforms of FC-HMMR when PF = 1 and 0.9, (a) delivered active and reactive power, (b) AC grid side voltages, (c) AC side currents, (d) DC voltage, (e) three-phase upper CL currents, (f) three-phase lower CL currents, (g) phase *a* upper and lower CL output voltages, (h) three-phase flying capacitor voltages, (i) phase *a* upper and lower CL capacitor voltages.

Fig. 16 depicts the steady-state waveforms of FC-HMMR at a constant apparent power of 5 MW and PF of 1 and 0.9. The CL current waveforms align with the designed current pattern in Fig. 7. Additionally, the extra flying capacitor voltages are shown in Fig. 16(h), which indicates a higher voltage ripple at lower PF. In this case, the SM capacitance C_{SM} is selected as 6 mF.

The steady-state waveforms of AAAR are presented in Fig. 17. The active power and reactive power exhibit low-frequency harmonics, which result from the AC current distortions during the state-changing transients in Fig. 17(c). The CL current step change in Fig. 17(e) brings more challenges to the current loop. Similar to FC-HMMR, the CL capacitor voltage ripple becomes larger at a lower PF. Moreover, the common-mode voltage with DC bias and third-order harmonics indicates the necessity of the three-phase transformer.

In Fig. 18, the dynamic performance and reactive power generation capability of FC-HMMR are demonstrated. The apparent power reference and PF are reduced simultaneously to ensure that the voltage ripple of CL and flying capacitor does not exceed the limitations. During the transient, the CL voltage stress does not change, indicating that extra devices are not required. Therefore, FC-HMMR exhibits greater flexibility than HMMR in terms of its ability to support the

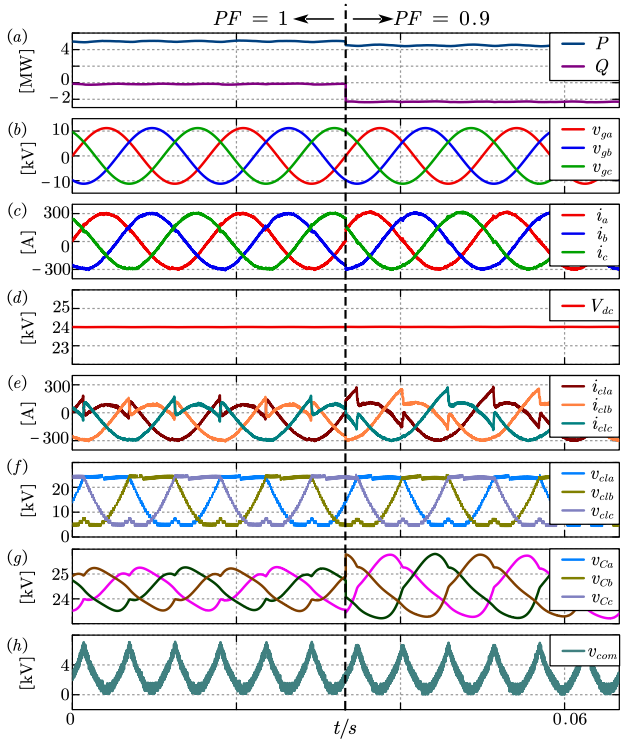

Fig. 17 Steady-state simulation waveforms of AAAR when PF = 1 and 0.9, (a) delivered active and reactive power, (b) AC grid side voltages, (c) AC side currents, (d) DC voltage, (e) three-phase CL currents, (f) three-phase CL output voltages, (g) phase a upper and lower CL capacitor voltages, (h) common-mode voltage v_{com}.

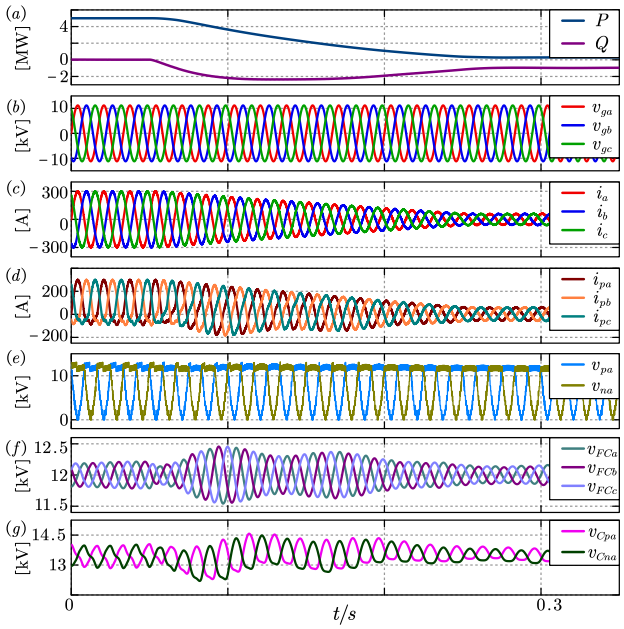

Fig. 18 Dynamic waveforms of FC-HMMR, (a) delivered active and reactive power, (b) AC grid side voltages, (c) AC side currents, (d) three-phase upper CL currents, (e) phase *a* upper and lower CL output voltages, (f) three-phase flying capacitor voltages, (g) phase *a* upper and lower CL capacitor voltages.

grid. It should be noted that the AAAR has the same capability compensate the reactive power from the grid, but the simulation is omitted here.

TABLE III
Electrical parameters of the experimental setup.

Parameters	Symbol	Values
AC voltage amplitude	V_{ac}	400 V
AC frequency	f_{ac}	60 Hz
Power factor	PF	0.8-1
DC output voltage	V_{dc}	800 V
DC resistor load	R_o	200 Ω
Arm inductance	L_{arm}	2 mH
SM voltage	V_{SM}	240 V
SM capacitance	C_{SM}	1 mF
Flying capacitance	C_{FC}	1 mF
Number of FB SM per CL	N_f	2
Switching frequency	f_c	12 kHz

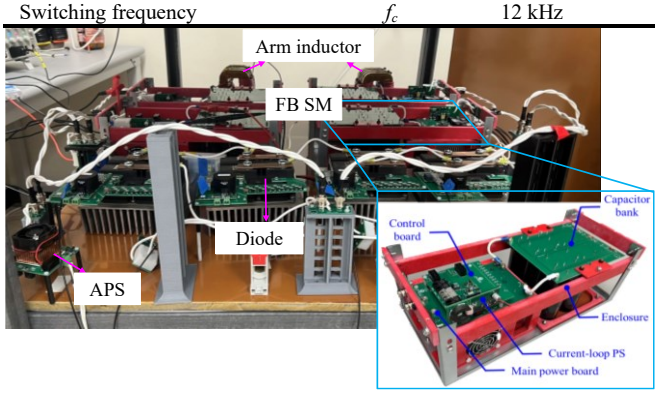

(a)

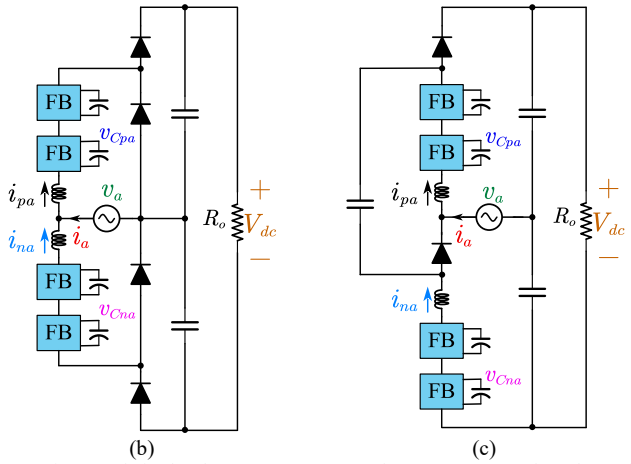

(b) (c)

Fig. 19 Picture of single-phase FC-HMMR and HMMR setup, (b) schematic of HMMR and (c) schematic of FC-HMMR.

B. Experimental Results

According to the comparison results, HMMR and FC-HMMR are the most promising HMRs to replace the traditional MMC. Consequently, a sub-scale single-phase prototype was constructed to validate HMMR and FC-HMMR, as shown in Fig. 19, with its parameters listed in Table III. However, AAAR was not tested here due to the incapability for the single-phase operation.

The FB SM is constructed with four 1.7 kV discrete Silicon Carbide (SiC) MOSFETs (G3R20MT17K) for high switching frequency to reduce the CL current ripple. All PWM signals, SM fault signals, SM capacitor voltage information, and sensor output are transmitted through the fiber. In this setup, the antiparallel diode of the 4.5 kV IGBT module (CM600HG-90H) is used as the HV diode. The current loop power supply [43], [44] is employed to provide the auxiliary power for four SMs, two CL current sensors, and two voltage sensors. As for the centralized system controller, the DSP (TMS320F28379) and FPGA (5CEFA4F23C8N) are used in this setup. The former is responsible for the control algorithm execution, while the latter generates all the PWM signals and receive the feedback value from sensors. We have added this part in the setup introduction.

The performance of HMMR has been extensively evaluated using steady-state and dynamic waveforms on a low-voltage prototype, as presented in [27]. In this paper, two tests of HMMR at PF of 1 and 0.8 are replicated on a higher voltage and power setup with the corresponding waveforms in Fig. 20. FB SMs are necessary here to generate the negative voltage in the case of non-unity PF. It shows similar waveforms in Fig. 15.

The steady-state results of FC-HMMR at PF = 1 and 0.8 are presented in Fig. 21(a) and Fig. 21(b), respectively. It can be observed that the AC input current has low harmonics, which indicates a well-designed current loop. Additionally, it is noticeable that the SM capacitor voltage ripple increases as the PF changes from 1 to 0.8. This outcome is consistent with the relationship presented in Fig. 13 and the simulation waveform demonstrated in Fig. 16. The DC output voltage closely

follows the reference of 800 V due to the DC voltage balancing shown in Fig. 10(a).

TABLE IV
Efficiency Test Results of Four cases.

Condition	HMMR		FC-HMMR	
	PF = 1	PF =0.8	PF = 1	PF = 0.8
Efficiency	98.4%	97.2%	97.8%	95.9%

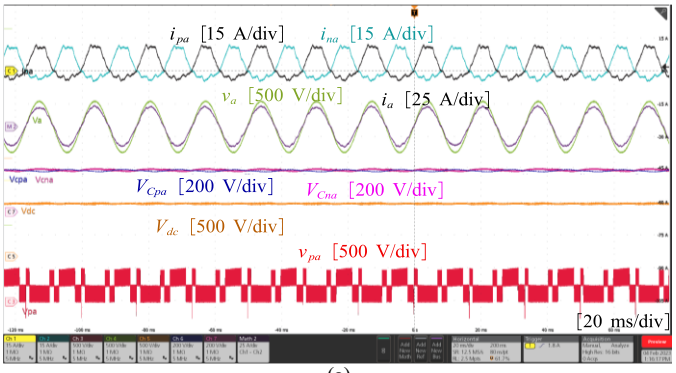

(a)

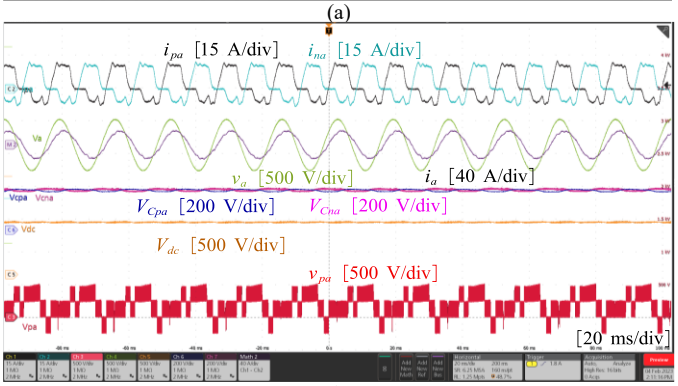

(b)

Fig. 20 Steady-state waveforms of HMMR with (a) PF = 1, and (b) PF = 0.8.

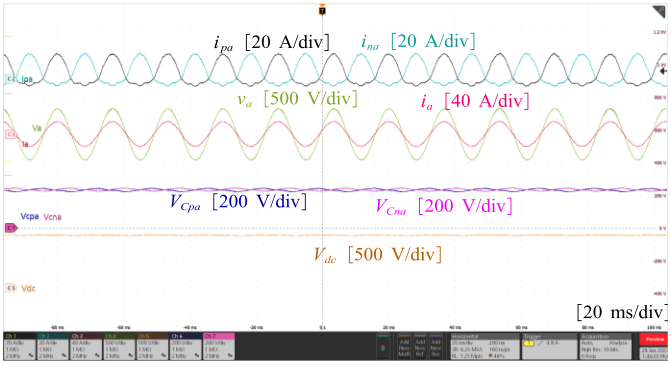

(a)

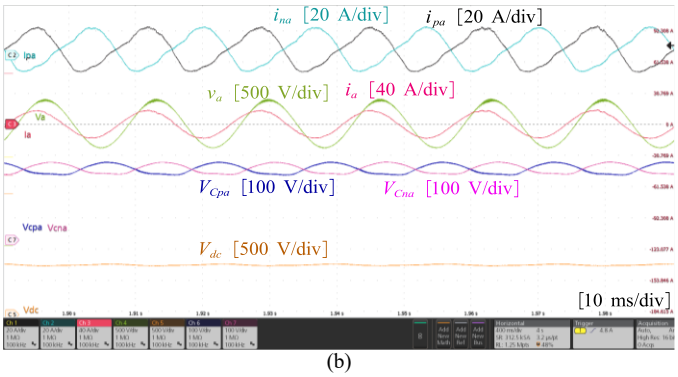

(b)

Fig. 21 Steady-state waveforms of FC-HMMR with (a) PF = 1, and (b) PF = 0.8.

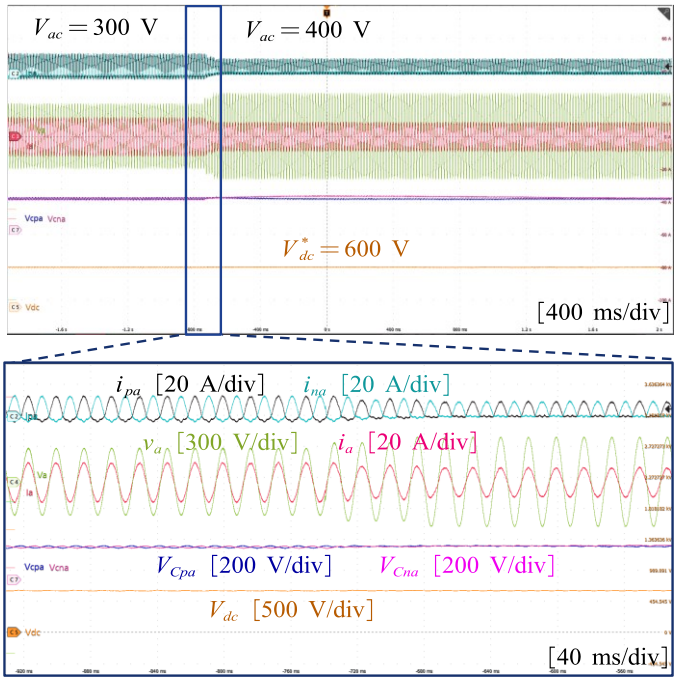

Fig. 22 Dynamic waveforms of FC-HMMR when AC input voltage amplitude increases from 600V to 800 V.

To evaluate the dynamic performance of FC-HMMR, the AC input voltage was instantly increased from 300 V to 400 V, and the resulting waveforms are shown in Fig. 22. Both before and after the transient, the DC voltage follows the reference value of 600 V, demonstrating the effectiveness of the output voltage control. Furthermore, the results indicate that FC-HMMR can also function as a step-down rectifier when the FB SM is employed. The CL capacitor voltages merge after the transient due to the energy balancing scheme. Additionally, it could be observed that HMMR exhibits a lower SM capacitor voltage ripple compared to FC-HMMR. The efficiency test results are given in Table IV, which validates the tendency of Fig. 14.

VI. Conclusions

In this paper, three representative HMRs are introduced for unidirectional power flow applications: HMMR, FC-HMMR,

and AAAR. These topologies were proposed to replace traditional MMC for higher efficiency and power density. Based on their unique operation principles, their performances are evaluated comprehensively to identify the advantages and limitations of each topology. It can be found that HMMR has the best performance in the high PF range due to the lowest capacitor size and power losses. Therefore, HMMR is desired in the ac-dc front-end converter in the marine various electrical power delivery and distribution systems and point-to-point HVDC transmission. If a large PF range is required, FC-HMMR and AAAR become a better solution, because they do not add extra devices compared to HMMR. Moreover, FC-HMMR does not need the three-phase transformer, which is required for AAAR to block the common-mode voltage. Nevertheless, considering the insulation capability of flying capacitor, the FC-HMMR is more suitable for MV applications such as FCS and datacenter based on dc distribution. If pure reactive power compensation is the target, the traditional MMC is still the best option.

Unbalanced operation is very important for the grid-connected HMRs, which should be different from MMC and deserve more investigation. Besides, techniques to improve the control performance and dynamic response for the HMRs are other interesting avenues for the future work.

Nowadays, more bidirectional HMCs are emerging, and their rectifier versions deserve more investigation and optimization. This will expand the family of HMRs, providing more options for unidirectional AC/DC power conversion.

ACKNOWLEDGMENT

This work was supported by the National Science Foundation under Grant 2022397. Any opinions, findings, and conclusions or recommendations expressed in this material are those of the author(s) and do not necessarily reflect the views of the NSF.

REFERENCES

[1] N. Flourentzou, V. G. Agelidis and G. D. Demetriades, "VSC-Based HVDC Power Transmission Systems: An Overview," in IEEE Transactions on Power Electronics, vol. 24, no. 3, pp. 592-602, March 2009.

[2] A. Nami, J. Liang, F. Dijkhuizen and G. D. Demetriades, "Modular Multilevel Converters for HVDC Applications: Review on Converter Cells and Functionalities," in IEEE Transactions on Power Electronics, vol. 30, no. 1, pp. 18-36, Jan. 2015.

[3] G. J. M. de Sousa and M. L. Heldwein, "Modular multilevel converter based unidirectional medium/high voltage drive system," IECON 2013 - 39th Annual Conference of the IEEE Industrial Electronics Society, 2013, pp. 1037-1042.

[4] W. Yang, Q. Song, S. Xu, H. Rao and W. Liu, "An MMC Topology Based on Unidirectional Current H-Bridge Submodule With Active Circulating Current Injection," in IEEE Transactions on Power Electronics, vol. 33, no. 5, pp. 3870-3883, May 2018.

[5] G. J. M. de Sousa and M. L. Heldwein, "Three-phase unidirectional modular multilevel converter," 2013 15th European Conference on Power Electronics and Applications (EPE), 2013, pp. 1-10.

[6] E. Skjong, R. Volden, E. Rødskar, M. Molinas, T. A. Johansen and J. Cunningham, "Past, Present, and Future Challenges of the Marine Vessel's Electrical Power System," in IEEE Transactions on Transportation Electrification, vol. 2, no. 4, pp. 522-537, Dec. 2016.

[7] Wu, Bin, and Mehdi Narimani. High-power converters and AC drives. John Wiley & Sons, 2017.

[8] A. Nami, J. L. Rodriguez-Amenedo, S. Arnaltes, M. Á. Cardiel-Álvarez and R. A. Baraciarte, "Frequency Control of Offshore Wind Farm With Diode-Rectifier-based HVDC Connection," in IEEE Transactions on Energy Conversion, vol. 35, no. 1, pp. 130-138, March 2020.

[9] A. Nabae, I. Takahashi and H. Akagi, "A New Neutral-Point-Clamped PWM Inverter," in IEEE Transactions on Industry Applications, vol. IA-17, no. 5, pp. 518-523, Sept. 1981.

[10] H. Abu-Rub, J. Holtz, J. Rodriguez and G. Baoming, "Medium-Voltage Multilevel Converters—State of the Art, Challenges, and Requirements in Industrial Applications," in IEEE Transactions on Industrial Electronics, vol. 57, no. 8, pp. 2581-2596, Aug. 2010.

[11] X. Zhao et al., "An Enhanced Modulation Scheme for Multi-Level T-Type Inverter with Loss Balance and Reduction," in IEEE Transactions on Power Electronics, doi: 10.1109/TPEL.2023.3289508.

[12] Y. Zhang et al., "A SiC and Si Hybrid Five-Level Unidirectional Rectifier for Medium Voltage Applications," in IEEE Transactions on Industrial Electronics, vol. 69, no. 8, pp. 7537-7548, Aug. 2022.

[13] P. Zhang et al., "A Carrier-Based Discontinuous PWM Scheme With Optimal PWM Sequences for a Five-Level Flying Capacitor Rectifier," in IEEE Transactions on Power Electronics, vol. 37, no. 11, pp. 13178-13191, Nov. 2022.

[14] S. Chatterjee, D. Mukherjee and D. Kastha, "Loss Comparison of Various Unidirectional Rectifiers for Medium Voltage Applications," 2020 IEEE Calcutta Conference (CALCON), 2020, pp. 166-170.

[15] D. Bosich, R. A. Mastromauro and G. Sulligoi, "AC-DC interface converters for MW-scale MVDC distribution systems: A survey," 2017 IEEE Electric Ship Technologies Symposium (ESTS), Arlington, VA, USA, 2017, pp. 44-49.

[16] X. She, A. Q. Huang and R. Burgos, "Review of Solid-State Transformer Technologies and Their Application in Power Distribution Systems," in IEEE Journal of Emerging and Selected Topics in Power Electronics, vol. 1, no. 3, pp. 186-198, Sept. 2013.

[17] D. Dong, M. Agamy, J. Z. Bebic, Q. Chen and G. Mandrusiak, "A Modular SiC High-Frequency Solid-State Transformer for Medium-Voltage Applications: Design, Implementation, and Testing," in IEEE Journal of Emerging and Selected Topics in Power Electronics, vol. 7, no. 2, pp. 768-778, June 2019.

[18] J. K. Motwani, B. Fan, Y. Rong, D. Boroyevich, D. Dong and R. Burgos, "Closed-Loop Capacitor Voltage Balancing Scheme for Modular Multilevel Converters Operated in Switching-Cycle Balancing Mode," in IEEE Transactions on Power Electronics, vol. 38, no. 5, pp. 5603-5608, May 2023.

[19] W. Yang, Q. Song, S. Xu, H. Rao and W. Liu, "An MMC Topology Based on Unidirectional Current H-Bridge Submodule With Active Circulating Current Injection," in IEEE Transactions on Power Electronics, vol. 33, no. 5, pp. 3870-3883, May 2018.

[20] J. K. Motwani, J. Liu, R. Burgos, Z. Zhou and D. Dong, "Hybrid Modular Multilevel Converters for High-AC/Low-DC Medium-Voltage Applications," in IEEE Open Journal of Power Electronics, vol. 4, pp. 265-282, 2023.

[21] P. Bakas et al., "Review of Hybrid Multilevel Converter Topologies Utilizing Thyristors for HVDC Applications," in IEEE Transactions on Power Electronics, vol. 36, no. 1, pp. 174-190, Jan. 2021.

[22] J. K. Motwani, J. Liu, D. Boroyevich, R. Burgos and D. Dong, "A Comparative Evaluation between Hybrid Modular Multi-Level Converters and Alternate Arm Converter," 2023 IEEE 24th Workshop on Control and Modeling for Power Electronics (COMPEL), Ann Arbor, MI, USA, 2023, pp. 1-8.

[23] M. M. C. Merlin et al., "The extended overlap alternate arm converter: A voltage source converter with DC fault ride-through capability and a compact design," IEEE Trans. Power Electron., vol. 33, no. 5, pp. 3898–3910, May 2018.

[24] J. Liu, D. Dong and D. Zhang, "A Hybrid Modular Multilevel Converter Family With Higher Power Density and Efficiency," in IEEE Transactions on Power Electronics, vol. 36, no. 8, pp. 9001-9014, Aug. 2021.

[25] J. Liu, D. Zhang and D. Dong, "Modeling and Control Method for a Three-Level Hybrid Modular Multilevel Converter," in IEEE

Transactions on Power Electronics, vol. 37, no. 3, pp. 2870-2884, March 2022.
[26] J. Liu, D. Dong and D. Zhang, "Hybrid Modular Multilevel Rectifier: A New High-Efficient High-Performance Rectifier Topology for HVDC Power Delivery," in IEEE Transactions on Power Electronics, vol. 36, no. 8, pp. 8583-8587, Aug. 2021.
[27] J. Liu, D. Zhang and D. Dong, "Analysis of Hybrid Modular Multilevel Rectifier Operated at Nonunity Power Factor for HVDC Applications," in IEEE Transactions on Power Electronics, vol. 37, no. 9, pp. 10642-10657, Sept. 2022.
[28] J. Liu, J. K. Motwani, R. Burgos, Z. Zhou and D. Dong, "A New Hybrid Modular Multilevel Rectifier as MVac–LVdc Active Front-End Converter for Fast Charging Stations and Data Centers," in IEEE Transactions on Power Electronics, vol. 38, no. 9, pp. 11023-11037, Sept. 2023.
[29] J. Liu and D. Dong, "A Flying Capacitor Hybrid Modular Multilevel Converter With Reduced Number of Submodules and Power Losses," in IEEE Transactions on Industrial Electronics, vol. 70, no. 4, pp. 3293-3302, April 2023.
[30] D. Soto, F. Neira, R. Peña, R. Blasco-Gimenez and J. Riedemann, "Control Strategy for an AC/DC Asymmetric Alternate Arm Converter," 2018 20th European Conference on Power Electronics and Applications (EPE'18 ECCE Europe), 2018, pp. P.1-P.8.
[31] S. Yang, Y. Tang and P. Wang, "Distributed Control for a Modular Multilevel Converter," in IEEE Transactions on Power Electronics, vol. 33, no. 7, pp. 5578-5591, July 2018.
[32] W. Yao, J. Liu and Z. Lu, "Distributed Control for the Modular Multilevel Matrix Converter," in IEEE Transactions on Power Electronics, vol. 34, no. 4, pp. 3775-3788, April 2019.
[33] C. Burgos-Mellado et al., "Cyber-Attacks in Modular Multilevel Converters," in IEEE Transactions on Power Electronics, vol. 37, no. 7, pp. 8488-8501, July 2022.
[34] B. Xia et al., "Decentralized Control Method for Modular Multilevel Converters," in IEEE Transactions on Power Electronics, vol. 34, no. 6, pp. 5117-5130, June 2019.
[35] Infineon IGBT Module Manuals, 2023. [online] Available: https://www.infineon.com/cms/en/product/power/ibt/igbt-modules/.
[36] Littelfuse rectifier diode Manuals, 2023. [online] Available: https://www.littelfuse.com/products/power-semiconductors/discrete-diodes/rectifier/ rectifier-capsule-type.aspx#.
[37] W. Xiang, S. Yang, L. Xu, J. Zhang, W. Lin and J. Wen, "A Transient Voltage-Based DC Fault Line Protection Scheme for MMC-Based DC Grid Embedding DC Breakers," in IEEE Transactions on Power Delivery, vol. 34, no. 1, pp. 334-345, Feb. 2019.
[38] J. Liu et al., "12-kV 1-kA Breaking Capable Modular Power Electronic Interrupter With Staged Turn-off Strategy for Medium-Voltage DC Hybrid Circuit Breaker," in IEEE Transactions on Industry Applications, vol. 58, no. 5, pp. 6343-6356, Sept.-Oct. 2022.
[39] U. Javaid, F. D. Freijedo, D. Dujic and W. van der Merwe, "MVDC supply technologies for marine electrical distribution systems," in CPSS Transactions on Power Electronics and Applications, vol. 3, no. 1, pp. 65-76, March 2018.
[40] Y. Cao, M. Ngo, N. Yan, Y. Bai, R. Burgos and D. Dong, "DC Distribution Converter with Partial Power Processing for LVDC/MVDC Systems," 2021 IEEE Fourth International Conference on DC Microgrids (ICDCM), Arlington, VA, USA, 2021, pp. 1-8.
[41] T. Yuan, F. Jin, Z. Li, C. Zhao and Q. Li, "Design of an Integrated Transformer with Parallel Windings for a 30-kW LLC Resonant Converter," in IEEE Transactions on Power Electronics, doi: 10.1109/TPEL.2023.3291954.
[42] Y. Chang and X. Cai, "Hybrid Topology of a Diode-Rectifier-Based HVDC System for Offshore Wind Farms," in IEEE Journal of Emerging and Selected Topics in Power Electronics, vol. 7, no. 3, pp. 2116-2128, Sept. 2019.
[43] N. Yan, D. Dong and R. Burgos, "A Multichannel High-Frequency Current Link Based Isolated Auxiliary Power Supply for Medium-Voltage Applications," in IEEE Transactions on Power Electronics, vol. 37, no. 1, pp. 674-686, Jan. 2022.
[44] J. Hu, J. Wang, R. Burgos, B. Wen and D. Boroyevich, "High-Density Current-Transformer-Based Gate-Drive Power Supply With Reinforced Isolation for 10-kV SiC MOSFET Modules," in IEEE Journal of Emerging and Selected Topics in Power Electronics, vol. 8, no. 3, pp. 2217-2226, Sept. 2020.

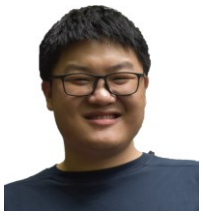

Jian Liu (Student Member, IEEE) received the B.S. and M.S. degrees in electrical engineering from Zhejiang University, Hangzhou, China, in 2016 and 2019, respectively, and the Ph.D. degree in electrical engineering from Virginia Tech, Blacksburg, VA, USA, in 2023.

He is currently a member of R&D staff with Delta Electronics, Inc., Research Triangle Park, NC, USA. His research interests include modular multilevel converter, medium-voltage solid-state transforms, etc.

Dr. Liu is the recipient of the best paper award of ECCE-Asia 2020 and the outstanding presentation award of APEC 2021.

Jayesh Kumar Motwani (Student Member, IEEE) received the Integrated Dual Degree (B.Tech. in electrical engineering and M.Tech. in power electronics) from the Department of Electrical Engineering, Indian Institute of Technology (B.H.U.), Varanasi, India, in 2020. He is currently working toward a Ph.D. degree at the Center for Power Electronics Systems, Virginia Tech, Blacksburg, VA, USA. He was a Visiting Scholar with the Politecnico di Milano, Milan, Italy, and Duke University, Durham, NC, USA, in 2018 and 2019, respectively, where he worked on modular converters. His research interests include modeling large power-electronic systems, control of modular power converters, integration of renewable energy systems, and wide-bandgap semiconductor applications. Mr. Motwani is the recipient of 3rd Prize Paper Award at IEEE International Power Electronics Conference, 2022.

Di Zhang (M'10–SM'16) received the B.S. and M.S. degrees from Tsinghua University, Beijing, China, in 2004 and 2006, respectively, and the Ph.D. degree from Virginia Tech, Blacksburg, VA, USA, in 2010, all in Electrical Engineering.

He is currently an Associate Professor with Naval Postgraduate School, Monterey, CA, USA. His research interests include the modeling and design of medium to high voltage power converters, SiC based high performance

power conversion, and power conversion system for grid, renewable, and aviation.

Dong Dong (S'09–M'12–SM'20) received the B.S. degree from Tsinghua University, China, in 2007, and the M.S. and Ph.D. degrees from Virginia Tech, Blacksburg, VA, USA, in 2009 and 2012, both in electrical engineering.

From 2012 to 2018, he was with GE Global Research Center (GRC), Niskayuna, NY, USA, as an Electrical Engineer. At GE, he participated in and led multiple technology programs including MV/HVDC power distribution and power delivery, SiC high-frequency high-power conversion systems, solid-state transformers, and energy storage system. He received multiple technology awards including GE silver and gold medallion patent awards and GE technology transition awards. Since 2018, he has been with the Bradley Department of Electrical and Computer Engineering, Virginia Tech. He has published over 45 referred journal publications and more than 100 IEEE conference publications. He currently holds 34 granted US patents. His research interests include wide-band-gap power semiconductor-based high frequency power conversion, soft-switching and resonant converters, high-frequency transformers, and MV and HV power conversion system for grid, renewable, and transportation applications. Dr. Dong is currently an Associate Editor for IEEE Transactions on Power Electronics. He received two Transaction Prize Paper Awards from the IEEE TRANSACTIONS ON POWER ELECTRONICS and IEEE TRANSACTIONS ON INDUSTRY APPLICATIONS, William Portnoy Prize Paper Award and Transportation Systems Prize Paper Award from IEEE IAS, and NSF CAREER award. He served as the Vice Chair of IEEE Industry Application Society Schenectady Region Chapter in 2017 and General Chair of IEEE International Conference on DC Microgrids in 2021.